



# Signal attenuation-compensated projection-resolved OCT angiography

JIE WANG,<sup>1,2</sup> TRISTAN T. HORMEL,<sup>1</sup> STEVEN T. BAILEY,<sup>1</sup>  
THOMAS S. HWANG,<sup>1</sup> DAVID HUANG,<sup>1,2</sup> AND YALI JIA<sup>1,2,\*</sup>

<sup>1</sup>Casey Eye Institute, Oregon Health & Science University, Portland, Oregon, USA

<sup>2</sup>Department of Biomedical Engineering, Oregon Health & Science University, Portland, Oregon, USA

\*jiaya@ohsu.edu

**Abstract:** Projection artifacts are a significant limitation of optical coherence tomographic angiography (OCTA). Existing techniques to suppress these artifacts are sensitive to image quality, becoming less reliable on low-quality images. In this study, we propose a novel signal attenuation-compensated projection-resolved OCTA (sacPR-OCTA) algorithm. In addition to removing projection artifacts, our method compensates for shadows beneath large vessels. The proposed sacPR-OCTA algorithm improves vascular continuity, reduces the similarity of vascular patterns in different plexuses, and removes more residual artifacts compared to existing methods. In addition, the sacPR-OCTA algorithm better preserves flow signal in choroidal neovascular lesions and shadow-affected areas. Because sacPR-OCTA processes the data along normalized A-lines, it provides a general solution for removing projection artifacts agnostic to the platform.

© 2023 Optica Publishing Group under the terms of the [Optica Open Access Publishing Agreement](#)

## 1. Introduction

Optical coherence tomography angiography (OCTA) provides powerful means to image retinal vasculature down to the capillary scale [1,2]. Because it is based on OCT data, OCTA inherits many advantages of OCT imaging: non-invasive, depth-resolved, high-resolution, rapid, and inexpensive. These qualities mean that OCTA and its metrics could be deployed as routine screening tools to improve the management of retinal vascular disorders. OCTA-based metrics such as retinal vessel density and non-perfusion area correlate highly with disease severity in multiple prevalent blinding diseases [3–9], and OCTA can detect other key pathologies, such as choroidal neovascularization [10] or polypoidal choroidal vasculopathy [11].

The depth resolution in OCTA is especially beneficial in feature detection and quantification. The ability to detect vascular changes within a specific plexus improves diagnostic utility [12] and can inform our understanding of the disease pathophysiology [13–15]. In theory, OCTA can provide a complete capillary-resolution vascular and anatomic description of the retina and choroid. In practice, it falls short. A key reason for this shortcoming is projection artifacts. The first attempts at projection artifact removal merely scaled and subtracted vascular patterns in superficial *en face* angiograms from posterior angiograms [16,17], which only worked for *en face* images and at the cost of creating a negative shadow in posterior slabs, interrupting vessel continuity and affecting quantification as well as segmentation. As projection artifacts are volumetric artifacts, their removal should be performed on a voxel-by-voxel basis so that the whole volume can be viewed in either cross-section or *en face* orientation. This is more difficult because the magnitude of the projection artifact within a voxel is not directly measurable and must be estimated using data statistics or optical principles. Our group introduced projection-resolved OCTA (PR-OCTA), which was the first attempt at removing the artifacts on a voxel-by-voxel basis by considering flow signal statistics alone [18] or in conjunction with the OCT reflectance signal [19]. However, neither of these approaches accounted for signal attenuation along the optical length (axial depth), which is also problematic for imaging posterior vascular layers. We observed that both true flow and projection artifact signal strengths are associated with the

reflectance signal strength [18–21]. In addition to the inherent reflectivity of different anatomic layers, the reflectance signal is modulated by attenuation due to light scattering and absorption. Thus, the projection artifact magnitude is dependent not only on the reflectivity of the tissue but also on the depth within the retina. This phenomenon can be visualized in uncorrected OCTA cross-sections, where the artifactual tails extending beneath real vessels gradually diminish and disappear.

Here, we report a new projection artifact removal approach, signal attenuation-compensated projection-resolved OCTA (sacPR-OCTA), that estimates projection artifact magnitude while modeling signal attenuation. This method removes projection artifacts and can enhance the true flow signal under the large vessels, where the previous approaches had typically under/over processed the flow signal [18,19]. We assessed the algorithm's performance by quantifying vascular similarity between *en face* projections at different depths, vessel continuity, and the magnitude of residual artifacts. Together, these metrics provide a description of the degree to which artifacts are removed while the true flow is preserved. We also assessed algorithm performance on challenging scans with shadow artifacts caused by the pupillary edge or vitreous floaters, scans from different devices, and scans from eyes with various pathology. Our results indicate that the sacPR-OCTA achieves state-of-the-art projection artifact removal.

## 2. Data acquisition and pre-processing

This study was conducted in compliance with Declaration of Helsinki. Participants were scanned using three commercial spectral-domain OCTA systems: (1) RTVue-XR (Visionix/Optovue Inc., Fremont, CA) with a center wavelength of 840-nm and 70-kHz axial scan rate, (2) Solix (Visionix/Optovue Inc., Fremont, CA) with a center wavelength of 840-nm and 120-kHz axial scan rate, and (3) Angioplex (Carl Zeiss, Inc., Dublin, California) with a center wavelength of 840-nm and 68-kHz axial scan rate. In both RTVue-XR and Solix systems, the flow signal was detected using the commercial version of the split-spectrum amplitude-decorrelation angiography (SSADA) algorithm, which evaluates the reflectance variation between two consecutive B-scans acquired at the same position [1]. One X-fast and one Y-fast volume were obtained and registered to suppress motion artifacts [22]. The 3 × 3-mm and 6 × 6-mm scans were acquired using the RTVue-XR system, and 3 × 3-mm, 6 × 6-mm, 9 × 9-mm, and 12 × 12-mm scans were acquired using the Solix system. On the RTVue-XR system, a 3 × 3-mm volume consists of 304 B-scans, and each B-scan consists of 304 A-lines; and a 6 × 6-mm volume consists of 400 B-scans and each B-scan consists of 400 A-lines. With a faster scanning rate, the Solix system can achieve a higher scanning density with a 3 × 3-mm volume consisting of 400 B-scans and each consisting of 400 A-lines, a 6.4 × 6.4-mm volume consisting of 512 B-scans each with 512 A-lines, and 9 × 9-mm volumes consisting of 600 B-scans each with 600 A-lines. The Angioplex system detected the flows using optical microangiography (OMAG) algorithm [2]. A 3 × 3-mm Angioplex scan consists of 245 B-scans, and each B-scan consists of 245 A-lines.

A graph search-based algorithm segmented the boundaries between the vitreous and the inner limiting membrane (ILM); the ganglion cell layer (GCL) and the inner plexiform layer (IPL); IPL and the outer plexiform layer (OPL); OPL and the outer nuclear layer (ONL); and Bruch's membrane (BM) on structural OCT volume [23]. Segmentation errors were manually corrected using our custom Center for Ophthalmic Optics & Lasers lab OCTA reading toolkit (COOL-ART) software with intelligent manual correction. Applying retinal layers segmentation of structural OCT to OCTA volume, we generated maximum projection *en face* OCT angiograms of the superficial vascular complex (SVC), comprising the inner 80% of the ganglion cell complex (GCC); the intermediate capillary plexus (ICP), comprising the outer 20% of the GCC and inner 50% of the INL; the deep capillary plexus (DCP), comprising the outer 50% of the INL and OPL; the outer retina comprising the slab between the outer boundary of OPL and BM; and the choriocapillaris (CC), comprising the slab between the BM and BM + 10 μm.

### 3. Methods

#### 3.1. OCTA signal attenuation compensation

OCTA signal is generated by measuring the change in the amplitude (the magnitude of real and imaginary components), phase (the angle between the real and imaginary components), or complex signal (combining both amplitude and phase) from repeated structural B-scans acquired at the same location. Fluctuating shadows and multiple scattering of photons caused by the anterior moving blood cells detected as motion contrast produce projection artifacts, which appear as “tails” in cross-sections (Fig. 1(A)) and duplication of superficial vascular patterns in deeper anatomic slabs in *en face* images (Fig. 1(B-F)).

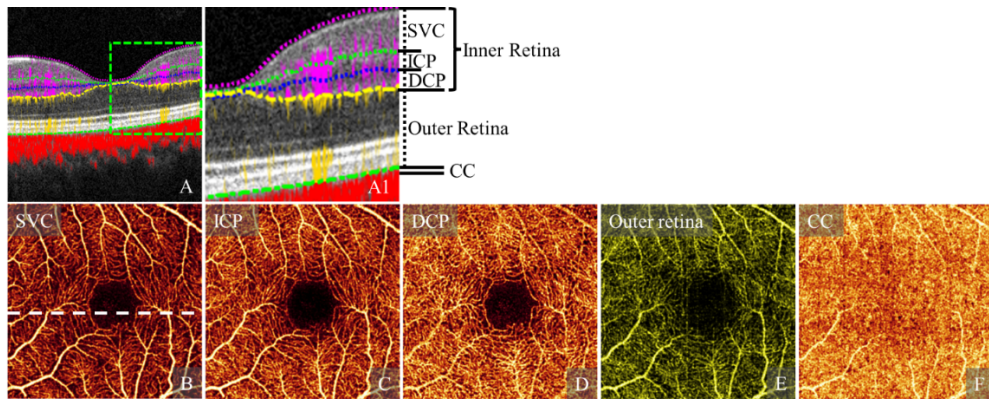


**Fig. 1.** Uncorrected OCTA with projection artifacts. (A) Cross-sectional OCT overlaid with color-coded OCTA signal (A) in the inner retina (violet), the outer retina (yellow), and the choroid (red) and the magnified view of the green box (A1). *En face* images are produced by maximum projection of the superficial vascular complex (SVC, B), intermediate capillary plexus (ICP, C), deep capillary plexus (DCP, D), the outer retina (E), and the choriocapillaries (F) slabs.

In this work, we model the observed flow signal within an A-line at depth  $z$  as the sum of contributions from true flow signal  $S_t(z)$ , flow signal from projection artifacts  $S_a(z)$ , and noise  $\sigma$  according to

$$S(z) = S_t(z) + S_a(z) + \sigma \quad (1)$$

However, we cannot directly measure any of the terms in (1) to recover  $S_t(z)$  from the observed signal  $S(z)$ , we define proportion coefficient  $p(z)$  such that

$$S_t(z) = p(z)S(z). \quad (2)$$

We observed that the averaged flow signal strength is around 6.1 and 3.4 times higher than the averaged noise strength on the healthy control scans acquired using Avanti and Zeiss Angioplex, respectively. Ignoring the noise contribution as it will be small relative to other terms, and further applying the Eq. (2) to (1), the observed flow signal  $S(z)$  can be written as

$$S(z) = p(z)S(z) + [1 - p(z)]S(z) \quad (3)$$

The task for projection artifact removal can therefore be equated to estimating  $p(z)$ , for which we require an estimate of  $S_a(z)$ . To obtain this, we begin by observing that projection artifact magnitude at depth  $z$  depends on both the inherent reflectivity  $R_{\text{OCT}}(z)$  of the tissue at that

location, and attenuation as the distance from the generating true flow  $d(z) = z - z_0$ . This yields

$$\begin{cases} A(z) = g[R_{\text{OCT}}(z), d(z)] \\ S_a(z) = A(z)S_t(z_0) \end{cases} \quad (4)$$

where  $g(\cdot)$  describes the functional dependence of the scaling coefficient for the artifactual signal relative to the true flow signal that produced it. To simplify, we assume that artifact strength scales linearly with the true flow signal. To proceed, we approximate (4) according to

$$\hat{S}_a(z) = \begin{cases} \left[ \alpha R_{\text{OCT}}(z) + \beta \left( 1 - \frac{d(z)}{d_{\max}} \right) \right] S_t(z_0), & \text{if } (z - z_0) \leq d_{\max} \\ \alpha R_{\text{OCT}}(z) S_t(z_0), & \text{if } (z - z_0) > d_{\max} \end{cases} \quad (5)$$

where  $\hat{S}_a(z)$  is the estimated projection artifact strength at depth  $z$ ,  $\alpha$  and  $\beta$  are fitted coefficients describing contributions from tissue reflectivity and artifact attenuation with depth, respectively, and  $d_{\max}$  (empirical parameter) restricts attenuation contributed by the optical path length. A soft process to enhance real flows was applied by

$$p(z) = \text{Nor}[S(z) - \hat{S}_a(z)] \quad (6)$$

The normalization, written as  $\text{Nor}(\cdot)$ , normalized the input in the range of 2.5 and 97.5 percentiles of elements to the range [0, 1].

Applying the Eq. (6) to the (2), the true flow  $S_t(z)$  can be restored by

$$S_t(z) = \begin{cases} \left\{ \text{Nor} \left\{ S(z) - \left[ \alpha R_{\text{OCT}}(z) + \beta \left( 1 - \frac{d(z)}{d_{\max}} \right) \right] S_t(z_0) \right\} \right\} S(z), & \text{if } (z - z_0) \leq d_{\max} \\ \left\{ \text{Nor} \left\{ S(z) - \alpha R_{\text{OCT}}(z) S_t(z_0) \right\} \right\} S(z), & \text{if } (z - z_0) > d_{\max} \end{cases} \quad (7)$$

where, the  $R_{\text{OCT}}(z)$  was normalized to [0, 1]. In implementation,  $\alpha$ ,  $\beta$  and  $d_{\max}$  were empirically determined in order to (1) maximize the vessel density in deeper slabs and (2) minimize pearson correlation between slabs. We suggested that  $\alpha$  and  $\beta$  should be restricted within the range of [0.2, 0.8], and the  $d_{\max}$  should be restricted in the range of [15, 62.5]  $\mu\text{m}$ .

### 3.2. Large vessel shadow compensation

Due to the light attenuation, large anterior vessels can produce shadow artifacts in posterior slabs. This complicates projection artifact removal since the shadow artifacts reduce image intensity. We, therefore, include extra processing in regions near such vessels. First, the retinal region (Fig. 2(B red)) is detected in the structural OCT channel using an adaptive thresholding [24,25]. We next generate an angiogram (Fig. 2(D)) covering the slab of ganglion cell complex (Fig. 2(C)) (corresponding to a 120  $\mu\text{m}$  axial depth, the average thickness of the ganglion cell complex [26]). Retinal vasculature is then enhanced using a vesselness filter [27] (Fig. 2(E1)). The vessel-enhanced image is then used to scale the original angiogram (Fig. 2(E2)). We obtain the large vessel mask by binarizing the scaled image using Otsu's method [28] and morphological operations (Fig. 2(F)). Voxel values in this large vessel mask are compensated by scaling according to the ratio of the surrounding tissue reflectivity to the area in the vessel mask, but only when signal attenuation occurs (i.e., when the voxels in the vessel area have lower reflectivity than the surrounding voxels). The surrounding voxels were selected as the nearest neighbors outside the large vessel mask at the same depth and 3 pixels width. Compared to the uncorrected cross-sectional OCT (Fig. 2(G1)), large vessel shadows were reduced (Fig. 2(G2)), allowing us to apply the proposed flow signal attenuation-compensated method (described in section 3.1) throughout the entire volume.

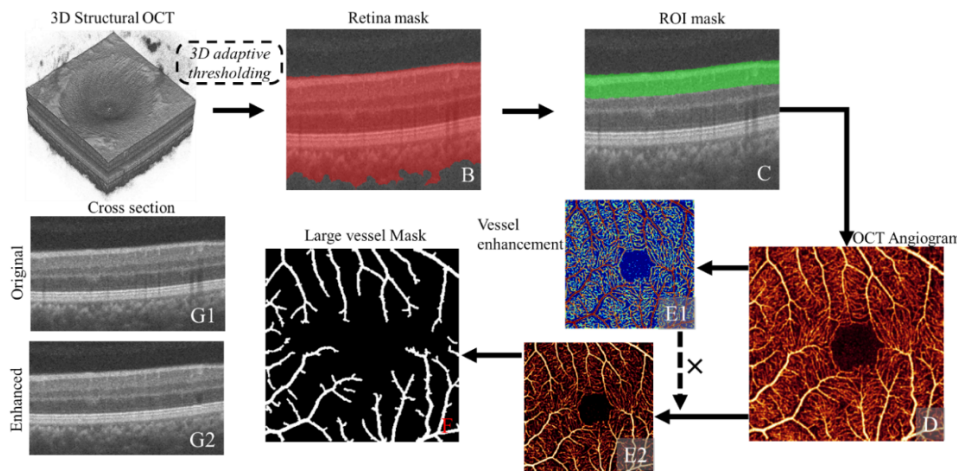


**Fig. 2.** Illustration of large vessel shadow compensation in structural OCT. (A) 3D structural OCT; (B) cross-section structural overlaid with a tissue mask (red) made using a 3D adaptive thresholding algorithm; (C) Cross-sectional structural OCT overlaid with the region of interested (ROI) mask (green) covering the slab of ganglion cell complex (corresponding to a 120  $\mu\text{m}$  axial depth); (D) OCT angiogram generated in the superficial region using maximum projection. (E1) enhanced vasculature; (E2) Denoised OCT angiogram generated by multiplying the enhanced vasculature (E1) with the original OCT angiogram (D); (F) Large vessel mask detected by using adaptive thresholding algorithm. (G1) Original cross-sectional OCT with shadowing artifacts under the large vessels; (G2) Shadowing artifacts compensated cross-sectional OCT.

### 3.3. Implementation

The proposed sacPR-OCTA algorithm was implemented using C++ and multithreading programming on the computer with Intel i9-10980XE CPU @ 3.00 GHz. An OCTA scan with standard resolution ( $640 \times 340 \times 304$ -pixel) was processed in 0.5 seconds.

## 4. Results

Visual inspection showed that compared to the uncorrected OCTA (Fig. 1), sacPR-OCTA removed projection artifacts volumetrically, with flow “tails” removed in the cross-sectional OCTA overlay (Fig. 3(D)), superficial vessel patterns (Fig. 3(A)) removed in intermediate (Fig. 3(B)) and deep (Fig. 3(C)) slabs, and the outer retina free of projection artifacts (Fig. 3(D)).

### 4.1. Evaluation on healthy eyes

In the uncorrected OCTA, projection artifacts appear as “tails” extending posteriorly from vessels in cross-section (Fig. 4(F1)) projecting vascular patterns in the SVC (Fig. 4(A1)) to the ICP (Fig. 4(B1)), the DCP (Fig. 4(C1)), the outer retina (which is normally avascular; Fig. 4(D1)), and the choriocapillaris (Fig. 4(E1)) in *en face* angiograms. Compared to the previous PR-OCTA algorithms [18,19] (Fig. 4(A2-F2), (A3-F3)), the sacPR-OCTA algorithm (Fig. 4(A4-F4)) preserved more flow signal and showed more complete microvascular patterns in all deeper vascular plexuses including the ICP (Fig. 4(B4)), DCP (Fig. 4(C4)) and CC (Fig. 4(E4)), especially in the areas’ posterior to large vessels, and suppressed projection artifacts more completely, showing a much cleaner outer retinal slab. In addition, the CC vasculature (Fig. 4(E4)) is more uniform using sacPR-OCTA than uncorrected OCTA (Fig. 4(E1)), initial

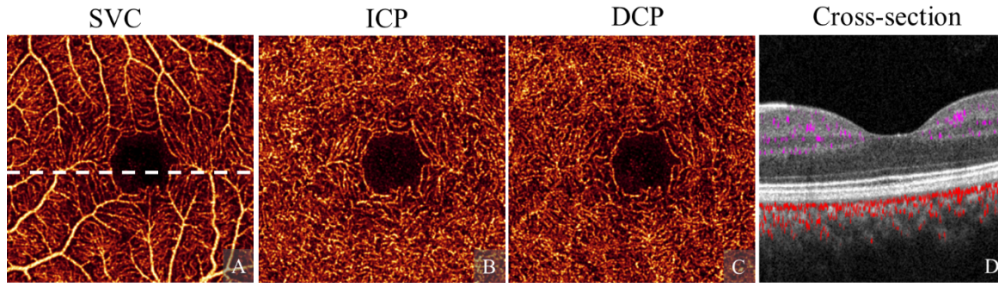


**Fig. 3.** Signal attenuation-compensated projection resolved OCTA (sacPR-OCTA) in a healthy eye, showing the superficial vascular complex (SVC, A), the intermediate capillary plexus (ICP, B), the deep capillary plexus (DCP, C) and a cross-sectional structural OCT overlaid with the sacPR-OCTA color-coded according to anatomic location (violet: inner retina, yellow: outer retina red: choroid; position was highlighted by the dotted line in A). The results reflect the known features of retinal vascular anatomy from the histology [29].

PR-OCTA (Fig. 4(E2)) [18] and reflectance-based projection-resolved OCTA (rbPR-OCTA) (Fig. 4(E3)) [19], closer to the histological description of the CC, making it more likely that biomarkers based on the CC reflects the actual changes in the CC.

For quantitative analysis, we assessed the vascular similarity between superficial and deeper slabs, vascular continuity, and residual artifacts strength ( $S_{RA}$ ) in the outer retina in 296 OCTA scans from 296 healthy eyes using the initial PR-OCTA [18], rbPR-OCTA [19] and sacPR-OCTA.

#### 4.1.1. Vascular similarity as a measurement of projection artifact removal

We measured vascular similarity using the Pearson's correlation coefficient ( $r$ ) [30] according to

$$r(I_A, I_B) = \frac{1}{N-1} \sum_{i=1}^N \left( \frac{I_A(i) - u_A}{\sigma_A} \right) \left( \frac{I_B(i) - u_B}{\sigma_B} \right) \quad (8)$$

where,  $I_A$ . and  $I_B$  are images A and B respectively,  $i$  is the index of pixel,  $N$  is the total number of pixels,  $u_A$  and  $u_B$  are intensity average of objects A and B, respectively;  $\sigma_A$ . and  $\sigma_B$  are standard deviations of objects A and B, respectively. Pearson's correlation coefficient is bounded between -1 and 1, with an  $r$  value of -1 indicating perfect negative correlation, a  $r$  value of 0 indicating no correlation, and a  $r$  value of 1 indicating perfect correlation.

Pearson's correlation coefficient  $r$  measures the removal of duplicated vascular patterns in the deeper slabs. An  $r$  value close to 0 demonstrates better performance for removing the projection artifacts. A negative  $r$  means bright voxels were replaced with 0, which is also artifactual, causing disrupted vascular integrity. The circular area with 1-mm diameter centered on the FAZ was excluded from evaluations. Projection artifacts in the uncorrected OCTA produce a high  $r$  in the ICP and DCP (Table 1). Compared to the uncorrected OCTA, the vascular similarity was significantly reduced ( $p < 0.01$ , t-test) with initial PR-OCTA, rbPR-OCTA, or sacPR-OCTA (Table 1). Initial PR-OCTA produced low ICP and DCP correlations. However, the negative  $r$  in the DCP ( $r = -0.11$ ) indicates that the true flow signals were overprocessed, generating shadowgraphic artifacts in deeper slabs. This effect was less pronounced with the rbPR-OCTA method. Compared to rbPR-OCTA, the sacPR-OCTA showed a significant reduction of vascular similarity in the ICP ( $p < 0.01$ , t-test). While the  $r$  of sacPR-OCTA was slightly higher than rbPR-OCTA in the DCP ( $p < 0.01$ , t-test), the duplicated vascular patterns were also largely removed ( $r = 0.16$ ). The lower similarity in the DCP achieved by rbPR-OCTA, however, does not necessarily indicate that the sacPR-OCTA method removed fewer projection artifacts. In fact, we expect some similarity between anterior and posterior retinal layers because somflow values

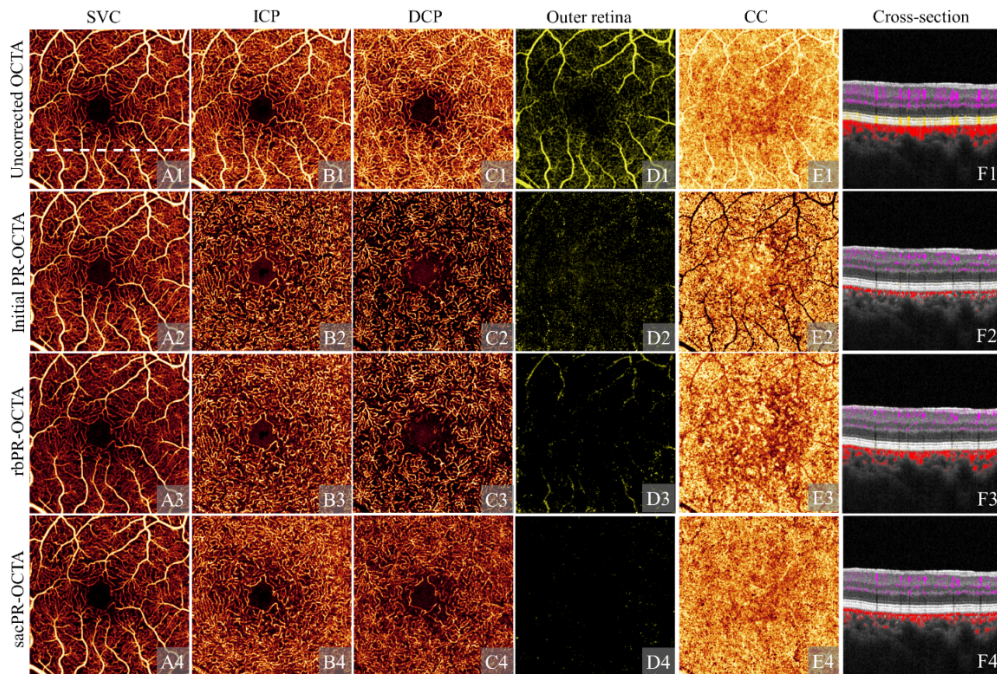


**Fig. 4.** A normal eye imaged with uncorrected OCTA (row 1), initial projection-resolved OCTA (PR-OCTA; row 2), reflectance-based projection-resolved OCTA (rbPR-OCTA, row 3), and the signal attenuation-compensated projection-resolved OCTA (sacPR-OCTA, row 4) showing *en face* OCT angiogram of the superficial vascular plexus (SVC, column A), the intermediate capillary plexus (ICP, column B), the deep capillary plexus (DCP, column C), the outer retina (column D) and the choriocapillaris (CC, column E), and the cross-sectional structural OCT overlaid with color-coded flow signal (column F; violet: inner retina, yellow: outer retina red: choroid) at the position indicated by the white dotted line in A1. The sacPR-OCTA removed more residual artifacts than the previous methods while maintaining vascular integrity, and volumetrically reduced the artifactual “tails” vessel tails (F1) with more anatomically correct circular shapes (F4) in cross-sectional OCTA. With both initial PR-OCTA and rbPR-OCTA, the flow signal is reduced under the larger vessels, particularly in the DCP and the CC (C2, E2, C3, E3). These overprocessing artifacts are absent in the proposed sacPR-OCTA method (C4, E4), which show uniform vascular patterns in the DCP and the CC.

will be similar. The very low similarity in rbPR-OCTA may be due to overprocessing resulting in the removal of some of the true flow signal. A visual inspection indicates that initial PR-OCTA and rbPR-OCTA algorithms had more fragmentation of vessel patterns, while the sacPR-OCTA did not result in more residual artifacts (Fig. 4).

#### 4.1.2. Vascular integrity and continuity as measurements of true flows preservation

We measured vascular integrity by calculating the vessel density defined by the ratio of the vascular pixels to the whole image. Vascular continuity was measured by vascular skeleton connectivity, which was defined as the ratio of the number of connected skeletonized pixels (more than 5 pixels connected if their edges or corners touch) to the total number of skeletonized pixels. The vascular binary mask was generated after applying the Frangi vesselness filter [27], which has been frequently used for vessel density quantification on OCTA. This filter can enhance the vasculature and suppress the background noise according to the local contrast measured using the

**Table 1. Comparison of Pearson's correlation coefficient between the SVC and the deeper vascular plexuses using uncorrected OCTA, initial projection-resolved OCTA (PR-OCTA), reflectance-based PR-OCTA (rbPR-OCTA), and signal attenuation-compensated PR-OCTA (sacPR-OCTA).<sup>a</sup>**

	Uncorrected OCTA	Initial PR-OCTA	rbPR-OCTA	sacPR-OCTA
ICP	0.70 ± 0.04	0.04 ± 0.09	0.21 ± 0.07	0.15 ± 0.06
DCP	0.53 ± 0.08	-0.11 ± 0.02	0.07 ± 0.08	0.16 ± 0.07

<sup>a</sup>ICP: Intermediate capillary plexus; DCP: Deep capillary plexus

Hessian matrix (Fig. 1(E1)). Then the vascular skeleton mask was obtained using the thinning methodology algorithm [31,32]. The circular area with 1-mm diameter centered on the FAZ was excluded from evaluations. For a fair comparison, the dynamic range of the OCT angiograms was truncated and normalized to the interval [0, 1] before applying the vesselness filter according to

$$I_{\text{nor}} = \begin{cases} 0 & I \leq I_{\min} \\ \frac{I - I_{\min}}{I_{\max} - I_{\min}} & I_{\min} < I < I_{\max} \\ 1 & I \geq I_{\max} \end{cases} \quad (9)$$

where,  $I_{\min}$  and  $I_{\max}$  are the 2.5 and 97.5 percentiles of elements in input  $I$ , respectively.

The sacPR-OCTA algorithm showed significant improvements (Table 2) in VD in deeper slabs ( $p < 0.01$ , t-test), indicating it preserved more of the true flow signal. It is possible that residual projection artifacts can also increase VD. However, both visual inspection and the low Pearson's correlation coefficient (Table 1) in the sacPR-OCTA method indicated that this was not the case. The higher VD in sacPR-OCTApared to rbPR-OCTA appears to be due to the improved preservation of the true flow signal. The higher vascular skeletonized connectivity indicates better performance of the sacPR-OCTA approach for preserving the vascular integrity (Table 2).

**Table 2. Comparison of vascular integrity and continuity using uncorrected OCTA, initial projection-resolved OCTA (PR-OCTA), reflectance-based PR-OCTA (rbPR-OCTA), and signal attenuation-compensated PR-OCTA (sacPR-OCTA).<sup>a</sup>**

	ICP		DCP	
	VD	VC	VD	VC
Uncorrected OCTA	0.55 ± 0.04	0.99 ± 0.00	0.57 ± 0.03	0.99 ± 0.00
Initial PR-OCTA	0.39 ± 0.03	0.95 ± 0.01	0.37 ± 0.04	0.94 ± 0.02
rbPR-OCTA	0.43 ± 0.08	0.98 ± 0.01	0.45 ± 0.06	0.97 ± 0.00
sacPR-OCTA	0.55 ± 0.02	0.98 ± 0.00	0.56 ± 0.02	0.98 ± 0.01

<sup>a</sup>ICP: Intermediate capillary plexus; DCP: Deep capillary plexus; VD: Vessel density; VC: Vascular continuity.

#### 4.1.3. Residual projection artifact signal strength in the outer retina

Residual projection artifact signal strength ( $S_{RA}$ ) in the outer retina, which is important for the accurate detection and quantification of choroidal neovascularization (CNV) in the normally avascular outer retina, was evaluated by

$$S_{RA} = \frac{M_{\text{outer}} + 3 \times \sigma_{\text{outer}}}{M_{\text{inner}} + 3 \times \sigma_{\text{inner}}} \quad (10)$$

where  $M_{\text{outer}}$  and  $M_{\text{inner}}$  are the mean and  $\sigma_{\text{outer}}$  and  $\sigma_{\text{inner}}$  are standard deviation in outer and inner retina, respectively.

The low  $S_{RA}$  demonstrates that the rbPR-OCTA and sacPR-OCTA removed the projection artifacts effectively in the outer retina of healthy eyes (Table 3).

**Table 3. Comparison of residual projection artifacts ( $S_{RA}$ ) in outer retina using uncorrected OCTA, initial projection-resolved OCTA (PR-OCTA), reflectance-based PR-OCTA (rbPR-OCTA) and signal attenuation-compensated PR-OCTA (sacPR-OCTA).**

Uncorrected OCTA	Initial PR-OCTA	rbPR-OCTA	sacPR-OCTA
$0.94 \pm 0.11$	$0.62 \pm 0.19$	$0.32 \pm 0.08$	$0.31 \pm 0.07$

#### 4.1.4. Evaluation of projection artifacts removal posterior to large vessels

The projection artifacts due to large vessels are more visually obvious due to the coincident shadow artifacts, which makes projection artifact removal under large vessels more challenging. We used Pearson's correlation coefficient  $r$  and VD to evaluate the performance of artifact removal under large vessels.

In the uncorrected OCTA, the correlation  $r$  is high in both the ICP and DCP (Table 4). A higher value  $r$  in the ICP compared to that of the DCP indicates that projection artifacts are stronger in the ICP (Fig. 4(B1)) than the DCP (Fig. 4(C1)). The negative correlation values of the initial PR-OCTA indicate that it overprocessed true flow signals generating shadowgraphic artifacts (Fig. 4(B2) & (C2)). Both the rbPR-OCTA and sacPR-OCTA algorithms produced low correlations, which indicate that they moved most of the projection artifacts in the deep slabs (Table 4). However, the VD is much higher with sacPR-OCTA ( $p < 0.01$ ), indicating sacPR-OCTA preserved more of the true flow signal.

**Table 4. Correlation of flow and vessel density between SVC and the deeper vascular slabs under the large vessels in the uncorrected OCTA, initial projection-resolved OCTA (PR-OCTA), reflectance-based projection-resolved OCTA (rbPR-OCTA) and signal attenuation-compensated projection-resolved OCTA (sacPR-OCTA).<sup>a</sup>**

	ICP		DCP	
	$r^+$	VD <sup>+</sup>	$r^+$	VD <sup>+</sup>
Uncorrected OCTA	$0.75 \pm 0.04$	$0.80 \pm 0.02$	$0.36 \pm 0.12$	$0.76 \pm 0.04$
Initial PR-OCTA	$-0.12 \pm 0.09$	$0.44 \pm 0.08$	$-0.33 \pm 0.05$	$0.28 \pm 0.06$
rbPR-OCTA	$-0.02 \pm 0.11$	$0.63 \pm 0.09$	$-0.04 \pm 0.10$	$0.48 \pm 0.09$
sacPR-OCTA	$0.00 \pm 0.07$	$0.65 \pm 0.03$	$0.03 \pm 0.09$	$0.62 \pm 0.05$

<sup>a</sup>ICP: Intermediate capillary plexus; DCP: Deep capillary plexus; <sup>+</sup>: Metrics were measured in the area under the larger vessels.

#### 4.2. Preservation of true flow signal on scans affected by shadow artifacts

Shadow artifacts, common in clinical settings, attenuate true flow signal in affected areas (Fig. 5(C1)), and make it more difficult to remove projection artifacts in deeper slabs. The initial PR-OCTA method overprocessed the real slow signal and generated large vessel shadows in ICP (Fig. 5(B2)) and DCP (Fig. 5(C2)). Since the rbPR-OCTA algorithm relies on vascular contrast in structural OCT, which can disappear in shadow affected regions, it can also overprocess both the projection artifacts and real flow signal in these regions (Fig. 5(C3)). The sacPR-OCTA algorithm does not have this limitation, as it processes the flow signal by A-line instead of by region, preserving more capillaries in both ICP (Fig. 5(B4)) and DCP (Fig. 5(C4)). In addition,

sacPR-OCTA removed more projection artifacts (Fig. 5(C4)) than rbPR-OCTA (Fig. 5(C3)) and produced a clearer outer retinal slab (Fig. 5(D4)). The sacPR-OCTA also generated more uniform appearing CC, with better preservation flow signals under large vessels (Fig. 5(E4)). These regions were overprocessed by initial PR-OCTA (Fig. 5(E2)) and rbPR-OCTA (Fig. 5(E3)).

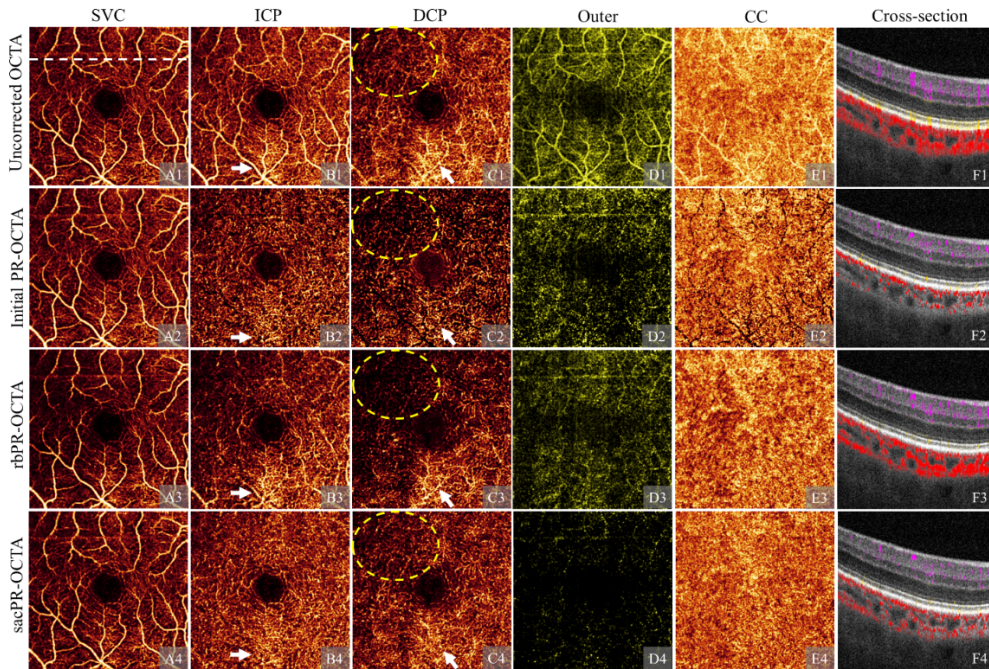


**Fig. 5.** A comparison of artifact suppression algorithms on a scan with shadow artifacts: uncorrected OCTA (row 1), initial projection-resolved OCTA (PR-OCTA, row 2), reflectance-based projection-resolved OCTA (rbPR-OCTA, row 3), and the signal attenuation-compensated projection-resolved OCTA (sacPR-OCTA, row 4) showing *en face* OCT angiogram of the superficial vascular plexus (SVC, column A), the intermediate capillary plexus (ICP, column B), the deep capillary plexus (DCP, column C), the outer retina (column D) and the choriocapillaris (CC, column E), and the cross-sectional structural OCT overlaid with color-coded flow signal (column F; violet: inner retina, yellow: outer retina red: choroid) The sacPR-OCTA algorithms preserved more of the true flow signal in the area affected by a shadow artifact (yellow dotted ellipses) and suppressed more projection artifacts (white arrows).

#### 4.3. Preservation of choroidal neovascularization

Choroidal neovascularization (CNV) consists of abnormal vessels in the outer retina. It causes vision loss through exudation, hemorrhage, fibrosis, and tissue damage [33–37]. OCTA as originally proposed, could detect CNV, but doing so was difficult due to the adjacent highly reflective retinal pigment epithelium, which produces strong projection artifacts (Fig. 6(D1)) [16]. These artifacts can both obscure real CNV or cause clinicians to misinterpret artifacts as CNV. Monitoring CNV with quantification is a clinical priority, but the artifacts make accurate quantification of CNV virtually impossible. The initial PR-OCTA (Fig. 6(D2)) and rbPR-OCTA (Fig. 6(D3)) algorithms could remove the artifacts, but the remaining background interfered with CNV quantification. In addition, the CNV produced visible projection artifacts in the CC of the uncorrected OCTA (Fig. 6(E1)), initial PR-OCTA (Fig. 6(E2)), and rbPR-OCTA results (Fig. 6(E3)). In addition to effectively removing artifacts in the inner (Fig. 6(A4–C4)) and outer

retinal slabs (Fig. 6(D4)), the sacPR-OCTA algorithm preserved more of the true CNV signal (Fig. 6(D4)), removed the projection onto the CC, and the shadows from large vessels (Fig. 6(E4)).

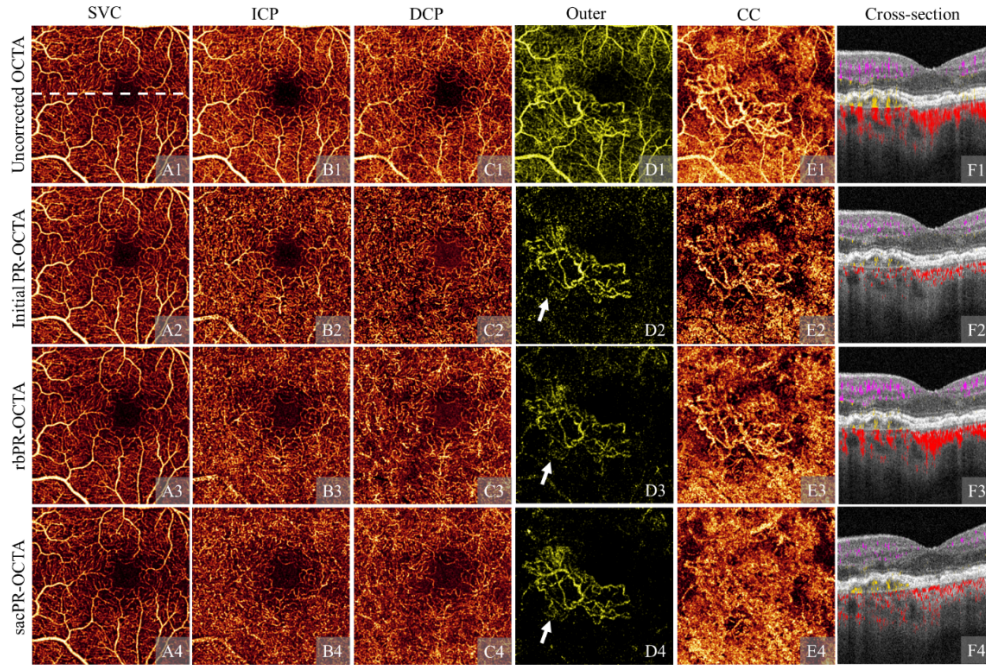


**Fig. 6.** A comparison of artifact removal algorithms on a scan with choroidal neovascularization (CNV): uncorrected OCTA (row 1), initial projection-resolved OCTA (PR-OCTA, row 2), reflectance-based projection-resolved OCTA (rbPR-OCTA, row 3), and the signal attenuation-compensated projection-resolved OCTA (sacPR-OCTA, row 4) showing *en face* OCT angiogram of the superficial vascular plexus (SVC, column A), the intermediate capillary plexus (ICP, column B), the deep capillary plexus (DCP, column C), the outer retina (column D) and the choriocapillaris (CC, column E), and the cross-sectional structural OCT overlaid with color-coded flow signal (column F; violet: inner retina, yellow: outer retina red: choroid) The proposed sacPR-OCTA algorithm preserved more of the true CNV signal (highlighted by white arrows).

#### 4.4. Platform independence

Since the proposed algorithm processes the flow signals on each A-line, it is theoretically independent of OCTA platform and the image resolution because it evaluates the proportion coefficient  $p(z)$  of the true flow signal on its own values. We tested the generalizability of the algorithm including platform and image-resolution independence on the Zeiss Angioplex OCTA and the Optovue Solix OCTA devices by refitting the three parameters  $\alpha$ ,  $\beta$  and  $d_{\max}$  in Eq. (7).

Independent of the platform, sacPR-OCTA could remove the projection artifacts, showing clear vasculature in deeper slabs (ICP&DCP, Fig. 7(B)&(C)), and suppressing the tailed projection artifacts (Fig. 7(D1)) voxel-wise (Fig. 7(D2)). It also preserved pathological nonperfusion areas and dilated vessel (Fig. 7(B2)&(C2)).

The faster imaging speed on Optovue Solix device allows a wider scan area with dense A-lines. The Solix macular 9 × 9-mm has 600 A-lines in each B-scan and 600 B-scans in each volume. With this field of view, it could detect neovascularization (NV) anterior to the internal limiting membrane that the previously standard 6 × 6-mm scans could not capture. The dense A-lines showed distinct NV vessels (Fig. 8(A1)). However, the projection artifacts obscured the

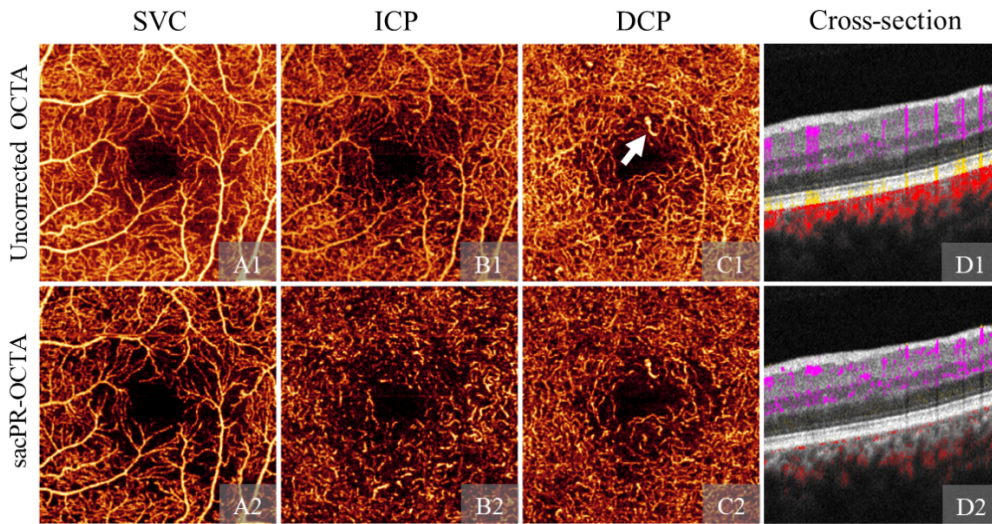


**Fig. 7.** Signal attenuation-compensated projection-resolved OCTA (sacPR-OCTA) on angioplex  $3 \times 3$ -mm scan. Row 1-2: Uncorrected OCTA and sacPR-OCTA. Column A-C are *en face* angiograms of the superficial vascular plexus (SVC), intermediate capillary plexus (ICP), deep capillary plexus (DCP). Column D is cross-sectional structural OCT overlaid with color-coded flow signals (violet: inner retina, yellow: outer retina red: choroid). The white arrow highlights the dilated vessel in DCP. sacPR-OCTA removes projection artifacts in this widely-used commercial device.

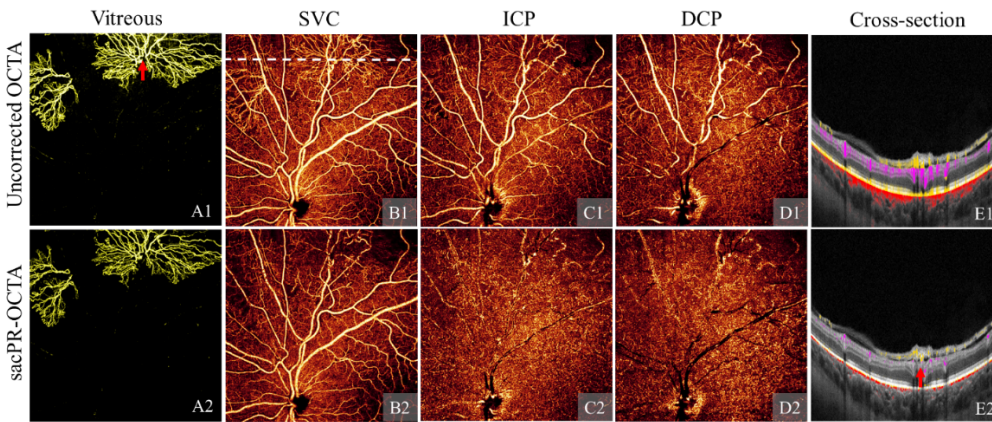


**Fig. 8.** Signal attenuation-compensated projection-resolved OCTA (sacPR-OCTA) on Solix  $9 \times 9$ -mm scan. Row 1-2: Uncorrected OCTA and sacPR-OCTA. Column A-D are *en face* angiograms of the neovascularization (NV) in the vitreous, superficial vascular plexus (SVC), intermediate capillary plexus (ICP), deep capillary plexus (DCP). Column E is cross-sectional structural OCT overlaid with color-coded flow signals (gold: vitreous, violet: inner retina, yellow: outer retina red: choroid). The red arrow highlights the connection between the NV and feeder vessel. sacPR-OCTA removed projection artifacts in this wide field of view showing the optic nerve head in a newly released commercial device.

underlying capillary dropout in the SVC (Fig. 8(B1)). The sac-PR-OCTA algorithm captured the NV and suppressed the projection artifacts, revealing distinct tortuous vessels in the SVC (Fig. 8(B2)) and the feeder vessels to the NV in cross-section (Fig. 8(E2)). However, a few

shadows due to overprocessing can be visualized on the DCP beneath the thick large vessels, which might be caused by two reasons (1) the OCTA algorithm was not able to detect this extremely weak flow signal (2) the contribution of true flow signal in the observed OCTA is very low. The simplified linear model is not complex enough to restore the weak flows, and the normalization procedure may also exclude them.

## 5. Discussion and conclusion

In this study, we developed a novel sacPR-OCTA algorithm that removes flow projection artifacts at the voxel level and preserves the true flow signal in OCTA. By improving on previous algorithms, this new algorithm can improve the visualization of retinal vasculature at all levels and the quantification of key disease metrics such as vessel density, non-perfusion area, and CNV area.

Several innovative features contributed to our approach's reliable performance. First, we based the algorithm on an improved theoretical foundation by considering not only the reflectivity of the tissue at the level of the artifact but also the signal attenuation with increasing distance from the true flow signal. Second, by using the theoretical form to fit the flow signal across the whole volume, our algorithm has the added advantage of enhancing the flow signal in regions posterior to large vessels which were under/over-processed by other projection-resolved algorithms. For the same reason, our algorithm better preserved the true flow signal in regions affected by shadow artifacts. Third, by processing the signal by A-line, the algorithm is independent of device, scan size, or resolution, making it generalizable.

A high-performing algorithm is expected to have the capability to remove projection artifacts and preserve the true flow signal. We used four quantitative metrics—Pearson's correlation coefficient, vessel density, vessel continuity, and remaining artifacts—to evaluate the performance of the sacPR-OCTA algorithm, as any one of them could not adequately describe its performance. Overprocessing can decrease correlation, while projection artifacts can increase vessel density and continuity. There is no straightforward answer as to whether one of these metrics should be independently optimized. For example, the deeper slabs could correlate less with the anterior slabs by removing more of the true flow signal. Thus, a lower correlation alone does not necessarily mean superior performance. Instead, only by evaluating the additional metrics—vessel density, vessel continuity, and remaining artifacts—we can obtain a complete picture of performance. We demonstrated that the sacPR-OCTA algorithm removed more projection artifacts (lower correlation and remaining artifact magnitude) while preserving more true flow (higher vessel density and connectivity).

Moreover, the sacPR-OCTA achieved cleaner backgrounds in the outer retina, even on scans affected by shadow artifacts, making quantitative measurements and clinical assessments on scans with sacPR-OCTA more reliable in real clinical settings. This is especially important in assessing CNV and nonperfusion areas [3,10,12,16,35,38].

The relationship between signal attenuation and reflectance and the optical distance is complicated. In our implementation, we simplified the complex dynamics using a linear model, which is a limitation of the proposed sacPR-OCTA. In the current model, the linear parameters can be adjusted individually to acquire the best OCTA. A non-linear model may improve projection artifact removal in OCTA further. One additional limitation of the proposed linear model is its inability to suppress background noise. This is because the model disregards the noise component. A non-linear model considering additional noise components may improve projection artifact removal in OCTA further.

**Funding.** National Institutes of Health (P30 EY010572, R01 EY023285, R01 EY024544, R01 EY027833, R01 EY031394, R01 EY035410, T32 EY023211, UL1TR002369); Research to Prevent Blindness (An Unrestricted Departmental Funding Grant and Dr. H. James and Carole Free Catalyst Award); Edward N. & Della L. Thome Memorial Foundation Award; Bright Focus Foundation (G2020168).

**Disclosures.** Jie Wang: Optovue/Visionix, Inc (P, R); David Huang: Optovue/Visionix, Inc. (F, P, R), Boeringer Ingelheim Inc. (C); Yali Jia: Optovue/Visionix, Inc. (P, R), Optos Inc. (P).

**Data availability.** The OCTA Data presented in this paper is not publicly available for download but may be obtained from the authors upon reasonable request.

## References

- Y. Jia, O. Tan, J. Tokayer, B. Potsaid, Y. Wang, J. J. Liu, M. F. Kraus, H. Subhash, J. G. Fujimoto, J. Horngger, and D. Huang, "Split-spectrum amplitude-decorrelation angiography with optical coherence tomography," *Opt. Express* **20**(4), 4710–4725 (2012).
- L. An and R. K. Wang, "In vivo volumetric imaging of vascular perfusion within human retina and choroids with optical micro-angiography," *Opt. Express* **16**(15), 11438–11452 (2008).
- T. S. Hwang, S. S. Gao, L. Liu, A. K. Lauer, S. T. Bailey, C. J. Flaxel, D. J. Wilson, D. Huang, and Y. Jia, "Automated quantification of capillary nonperfusion using optical coherence tomography angiography in diabetic retinopathy," *JAMA Ophthalmol.* **134**(4), 367–373 (2016).
- M. Zhang, T. S. Hwang, C. Dongye, D. J. Wilson, D. Huang, and Y. Jia, "Automated quantification of nonperfusion in three retinal plexuses using projection-resolved optical coherence tomography angiography in diabetic retinopathy," *Invest. Ophthalmol. Visual Sci.* **57**, 5101–5106 (2016).
- P. L. Nesper, B. T. Soetikno, and A. A. Fawzi, "Choriocapillaris nonperfusion is associated with poor visual acuity in eyes with reticular pseudodrusen," *Am. J. Ophthalmol.* **174**, 42–55 (2017).
- A. Y. Alibhai, L. R. De Pretto, E. M. Moult, C. Or, M. Arya, M. McGowan, O. Carrasco-Zevallos, B. Lee, S. Chen, and C. R. Baumal, "Quantification of retinal capillary nonperfusion in diabetics using wide-field optical coherence tomography angiography," *Retina* **40**(3), 412–420 (2020).
- Q. S. You, J. Wang, Y. Guo, C. J. Flaxel, T. S. Hwang, D. Huang, Y. Jia, and S. T. Bailey, "Detection of reduced retinal vessel density in eyes with geographic atrophy secondary to age-related macular degeneration using projection-resolved optical coherence tomography angiography," *Am. J. Ophthalmol.* **209**, 206–212 (2020).
- H. Akil, A. S. Huang, B. A. Francis, S. R. Sadda, and V. Chopra, "Retinal vessel density from optical coherence tomography angiography to differentiate early glaucoma, pre-perimetric glaucoma and normal eyes," *PLoS one* **12**(2), e0170476 (2017).
- M. B. Parodi, M. V. Cicinelli, A. Rabiolo, L. Pierro, M. Gagliardi, G. Bolognesi, and F. Bandello, "Vessel density analysis in patients with retinitis pigmentosa by means of optical coherence tomography angiography," *Br. J. Ophthalmol.* **101**(4), 428–432 (2017).
- J. Wang, T. T. Hormel, L. Gao, P. Zang, Y. Guo, X. Wang, S. T. Bailey, and Y. Jia, "Automated diagnosis and segmentation of choroidal neovascularization in OCT angiography using deep learning," *Biomed. Opt. Express* **11**(2), 927–944 (2020).
- M. Wang, Y. Zhou, S. S. Gao, W. Liu, Y. Huang, D. Huang, and Y. Jia, "Evaluating polypoidal choroidal vasculopathy with optical coherence tomography angiography," *Invest. Ophthalmol. Visual Sci.* **57**, OCT526 (2016).
- T. S. Hwang, A. M. Hagag, J. Wang, M. Zhang, A. Smith, D. J. Wilson, D. Huang, and Y. Jia, "Automated quantification of nonperfusion areas in 3 vascular plexuses with optical coherence tomography angiography in eyes of patients with diabetes," *JAMA Ophthalmol.* **136**(8), 929–936 (2018).
- F. Scarinci, P. L. Nesper, and A. A. Fawzi, "Deep retinal capillary nonperfusion is associated with photoreceptor disruption in diabetic macular ischemia," *Am. J. Ophthalmol.* **168**, 129–138 (2016).
- R. B. Rosen, J. S. A. Romo, B. D. Krawitz, S. Mo, A. A. Fawzi, R. E. Linderman, J. Carroll, A. Pinhas, and T. Y. Chui, "Earliest evidence of preclinical diabetic retinopathy revealed using optical coherence tomography angiography perfused capillary density," *Am. J. Ophthalmol.* **203**, 103–115 (2019).
- A. C. Onishi, P. L. Nesper, P. K. Roberts, G. A. Moharram, H. Chai, L. Liu, L. M. Jampol, and A. A. Fawzi, "Importance of considering the middle capillary plexus on OCT angiography in diabetic retinopathy," *Invest. Ophthalmol. Visual Sci.* **59**, 2167–2176 (2018).
- Y. Jia, S. T. Bailey, D. J. Wilson, O. Tan, M. L. Klein, C. J. Flaxel, B. Potsaid, J. J. Liu, C. D. Lu, and M. F. Kraus, "Quantitative optical coherence tomography angiography of choroidal neovascularization in age-related macular degeneration," *Ophthalmology* **121**(7), 1435–1444 (2014).
- A. Zhang, Q. Zhang, and R. K. Wang, "Minimizing projection artifacts for accurate presentation of choroidal neovascularization in OCT micro-angiography," *Biomed. Opt. Express* **6**(10), 4130–4143 (2015).
- M. Zhang, T. S. Hwang, J. P. Campbell, S. T. Bailey, D. J. Wilson, D. Huang, and Y. Jia, "Projection-resolved optical coherence tomographic angiography," *Biomed. Opt. Express* **7**(3), 816–828 (2016).
- J. Wang, M. Zhang, T. S. Hwang, S. T. Bailey, D. Huang, D. J. Wilson, and Y. Jia, "Reflectance-based projection-resolved optical coherence tomography angiography," *Biomed. Opt. Express* **8**(3), 1536–1548 (2017).
- S. S. Gao, Y. Jia, L. Liu, M. Zhang, H. L. Takusagawa, J. C. Morrison, and D. Huang, "Compensation for reflectance variation in vessel density quantification by optical coherence tomography angiography," *Invest. Ophthalmol. Visual Sci.* **57**, 4485–4492 (2016).
- A. Camino, Y. Jia, G. Liu, J. Wang, and D. Huang, "Regression-based algorithm for bulk motion subtraction in optical coherence tomography angiography," *Biomed. Opt. Express* **8**(6), 3053–3066 (2017).

22. M. F. Kraus, B. Potsaid, M. A. Mayer, R. Bock, B. Baumann, J. J. Liu, J. Hornegger, and J. G. Fujimoto, "Motion correction in optical coherence tomography volumes on a per A-scan basis using orthogonal scan patterns," *Biomed. Opt. Express* **3**(6), 1182–1199 (2012).
23. M. Zhang, J. Wang, A. D. Pechauer, T. S. Hwang, S. S. Gao, L. Liu, L. Liu, S. T. Bailey, D. J. Wilson, and D. Huang, "Advanced image processing for optical coherence tomographic angiography of macular diseases," *Biomed. Opt. Express* **6**(12), 4661–4675 (2015).
24. P. D. Wellner, "Adaptive thresholding for the DigitalDesk," Xerox, Technical Report EPC1993-110, 1–19 (1993).
25. D. Bradley and G. Roth, "Adaptive thresholding using the integral image," *Journal of graphics tools* **12**(2), 13–21 (2007).
26. O. Tan, V. Chopra, A. T.-H. Lu, J. S. Schuman, H. Ishikawa, G. Wollstein, R. Varma, and D. Huang, "Detection of macular ganglion cell loss in glaucoma by Fourier-domain optical coherence tomography," *Ophthalmology* **116**(12), 2305–2314.e2 (2009).
27. A. F. Frangi, W. J. Niessen, K. L. Vincken, and M. A. Viergever, "Multiscale vessel enhancement filtering," in *International Conference On Medical Image Computing and Computer-assisted Intervention* (Springer, 1998), pp. 130–137.
28. N. Otsu, "A threshold selection method from gray-level histograms," *IEEE transactions on systems, man, and cybernetics* **9**(1), 62–66 (1979).
29. C. Balaratnasingam, D. An, Y. Sakurada, C. S. Lee, A. Y. Lee, I. L. McAllister, K. B. Freund, M. Sarunic, and D.-Y. Yu, "Comparisons between histology and optical coherence tomography angiography of the periarterial capillary-free zone," *Am. J. Ophthalmol.* **189**, 55–64 (2018).
30. K. Pearson, "VII. Note on regression and inheritance in the case of two parents," *Proc. R. Soc. London* **58**(347–352), 240–242 (1895).
31. L. Lam, S.-W. Lee, and C. Y. Suen, "Thinning methodologies-a comprehensive survey," *IEEE Transactions on Pattern Analysis & Machine Intelligence* **14**, 869–885 (1992).
32. S. S. Gao, L. Liu, S. T. Bailey, C. J. Flaxel, D. Huang, D. Li, and Y. Jia, "Quantification of choroidal neovascularization vessel length using optical coherence tomography angiography," *J. Biomed. Opt.* **21**(7), 076010 (2016).
33. L. A. Donoso, D. Kim, A. Frost, A. Callahan, and G. Hageman, "The role of inflammation in the pathogenesis of age-related macular degeneration," *Surv. Ophthalmol.* **51**(2), 137–152 (2006).
34. P. E. Stanga, J. I. Lim, and P. Hamilton, "Indocyanine green angiography in chorioretinal diseases: indications and interpretation: an evidence-based update," *Ophthalmology* **110**(1), 15–21 (2003).
35. Q. Zhang, A. Zhang, C. S. Lee, A. Y. Lee, K. A. Rezaei, L. Roisman, A. Miller, F. Zheng, G. Gregori, and M. K. Durbin, "Projection artifact removal improves visualization and quantitation of macular neovascularization imaged by optical coherence tomography angiography," *Ophthalmology retina* **1**(2), 124–136 (2017).
36. F. Corvi, M. Cozzi, E. Barbolini, D. Nizza, M. Belotti, G. Staurenghi, and A. Giani, "Comparison between several optical coherence tomography angiography devices and indocyanine green angiography of choroidal neovascularization," *Retina* **40**(5), 873–880 (2020).
37. N. J. Y. Yeo, E. J. J. Chan, and C. Cheung, "Choroidal neovascularization: mechanisms of endothelial dysfunction," *Front. Pharmacol.* **10**, 1363 (2019).
38. J. Wang, T. T. Hormel, Q. You, Y. Guo, X. Wang, L. Chen, T. S. Hwang, and Y. Jia, "Robust non-perfusion area detection in three retinal plexuses using convolutional neural network in OCT angiography," *Biomed. Opt. Express* **11**(1), 330–345 (2020).